Dating protracted fault activities: microstructures, microchemistry and geochronology of the Vaikrita Thrust, Main Central Thrust zone, Garhwal Himalaya, NW India

Chiara Montemagni[1*], Chiara Montomoli[2], Salvatore Iaccarino[2], Rodolfo Carosi[3], Arvind K. Jain[4], Hans -J. Massonne[5] & Igor M. Villa[1,6]

1 - Dipartimento di Scienze dell'Ambiente e della Terra, Università di Milano Bicocca, Piazza della Scienza 4, 20126 Milano, Italy

2 - Dipartimento di Scienze della Terra, Università di Pisa, v. S. Maria 53, 56126 Pisa, Italy

3 - Dipartimento di Scienze della Terra, Università di Torino, v. Valperga Caluso 35, 10125, Torino, Italy

4 - CSIR-Central Building Research Institute, Roorkee -247667, Uttarakhand, India

5 - Institut für Mineralogie und Kristallchemie, Universität Stuttgart, Azenbergstraße 18, D-70049 Stuttgart, Germany

6 - Institut für Geologie, Universität Bern, Baltzerstrasse 3, 3012 Bern, Switzerland

*Corresponding author (c.montemagni@campus.unimib.it)

Short Title

Geochronology of the Vaikrita Thrust

Abstract

The timing of shearing along the Vaikrita Thrust, the structurally upper boundary of the Himalayan Main Central Thrust zone (MCTz), was constrained by combined microstructural, microchemical and geochronological investigations. Three different biotite-muscovite growth and recrystallisation episodes were observed: a relict mica-1; mica-2 along the main mylonitic foliation; mica-3 in coronitic structures formed around garnet during its breakdown.

Analyses of biotite with the electron microprobe show chloritisation, and bimodal composition of biotite-2 in one sample. Muscovite-2 and muscovite-3 have different compositions.

Biotite and muscovite ^{39}Ar-^{40}Ar age spectra from all samples give both inter-sample and intra-sample discrepancies. Biotite step ages range between 8.6 and 16 Ma, and muscovite step ages between 3.6 and >7 Ma. The obtained ages cannot be interpreted as "cooling ages", as samples from the same outcrop cooled simultaneously. Instead, Ar systematics reflect sample-specific recrystallisation markers. Intergrown impurities were diagnosed by Ca/K ratios. Age data of biotite were interpreted as mixture of true biotite-2 (9.00±0.10 Ma cooling age) and two alteration products. The negative Cl/K-age correlation identifies a Cl-poor muscovite-2 (>7 Ma) and a Cl-rich muscovite-3 (≤5.88±0.03 Ma). Coronitic muscovite grew at ≤5.88 Ma. The alteration of muscovite was minor to pervasive.

Constraining the age and duration of movements in shear zones is one of the major objectives in the study of the evolution of collisional belts (Challandes *et al*. 2003; Di Vincenzo *et al*. 2004; Carosi *et al*. 2006, 2010, 2016; Iaccarino *et al*., 2015; Rolland *et al*. 2009; Sanchez *et al*. 2011; Montomoli *et al*. 2013, 2015; Cottle *et al*. 2015), such as the Himalaya (Fig. 1a). One of the main unsolved problems in the Himalayan belt is the nature of the Main Central Thrust (MCT), a first-order tectonic discontinuity.

As discussed by Searle *et al*. (2008), Martin (2016) and Mukhopadhyay *et al*. (2017), the definition of the MCT has changed since the first one by Heim & Gansser (1939). The current debate is especially related to the criteria to define (and, thus, to localise) the MCT.

Therefore, several definitions of the MCT have been proposed (see Searle *et al*. 2008, and Martin 2016 for an updated review) such as (1) a structural-metamorphic (Heim & Gansser 1939); (2) a metamorphic-rheological (Searle *et al*. 2008) and rheological (e.g. Gibson *et al*. 2016; Parson *et al*. 2016); (3) a chronological (e.g. Webb *et al*. 2013); and (4) a compositional one, assuming that the MCT is a high-strain reverse kinematic zone that separates distinguishable protoliths (e.g. Martin *et al*. 2005; Martin 2016). Moreover, the MCT records a protracted deformation, from ductile to brittle (Carosi *et al*. 2007, and references therein), and affects several different lithologies along strike. This further complicates the debate.

The above controversy led to the definition of two distinct thrusts in NW India (Valdiya 1980; Ahmad *et al*. 2000; Saklani *et al*. 2001) and in Nepal (Hashimoto *et al*. 1973; Arita 1983; De Celles *et al*. 2000, Robinson *et al*. 2001; Robinson 2008). In different areas of the belt these two bounding thrusts have been named in different ways, although they refer to the same structural setting. In the Garhwal Himalaya (NW India), the MCTz is well exposed: Valdiya (1980) and Ahmad *et al*. (2000) defined the Munsiari Thrust at the bottom and the Vaikrita Thrust at the top of the MCTz, whereas Saklani *et al*. (1991) defined the lower thrust as MCT2 in the Yamuna valley in the Garhwal region. The activity time-span of the MCT in different areas of the belt was estimated in many mutually incompatible ways. This span ranges from 23-20 to 15 Ma in different areas of the belt (see Godin *et al*. 2006 and Montomoli *et al*. 2015 for an updated review) down to c. 3 Ma reported in central Nepal (Harrison *et al*. 1997; Catlos *et al*. 2001). In the Garhwal Himalaya, several authors proposed their preferred ages of the MCT activity based on different chronometers (K-Ar, Th-Pb and ^{39}Ar-^{40}Ar) and especially of different non-isotopic sample characterisations. Metcalfe (1993) suggested that in the Bhagirathi valley, about 100 km W of our study area (Fig. 1a), the MCT was active between 14 and 5.7 Ma, following K-Ar dating on biotite and muscovite. Catlos *et al*. (2002) extended their previous work on Nepal to western Garhwal beneath the Vaikrita Thrust and asserted that the Th-Pb ages of monazite constrain the age of the entire activity of the MCT in the central and western Himalaya to c. 6 Ma. Célérier *et al*. (2009) reported c. 9 Ma obtained (by ^{39}Ar-^{40}Ar on white mica) from samples in the middle portion of the MCTz near the village of Helang. Sen *et al*. (2015) obtained ^{40}Ar-^{39}Ar biotite data of c. 10 Ma and interpreted them as "cooling ages", which were correlated to the exhumation of the GHS caused by MCT thrusting at that time. In addition, muscovite ages of c. 6 Ma were related to a late stage deformation post-dating biotite cooling (Sen *et al*. 2015). However, questions concerning microstructural and chemical features in context with the protracted deformation have not been addressed by any of these conflicting studies.

As our observations of the deformation style of the MCTz in Garhwal strongly suggests a more complex history than that described in previous studies, we apply here an integrated structural-microchemical-geochronological approach (Vance *et al*. 2003) to provide a time frame for the different styles of activity of the Vaikrita thrust. The baseline for any interpretation is a detailed microstructural study (e.g. Rolland *et al*. 2009; Montomoli *et al*. 2013, 2015; Iaccarino *et al*., 2015), which is required to clarify the aforementioned contrasting estimates, as such a study can distinguish between pre-, syn-, and post- kinematic minerals. This can and should be linked to dated minerals applying analytical techniques that allow the recognition of heterochemical phases and simultaneously provide their age (e.g. analyses of monazite by the electron microprobe and of mica, amphibole and feldspar by ^{39}Ar-^{40}Ar mass spectrometry: Villa & Williams 2013; Villa & Hanchar 2017).

A recognition of heterochemical mineral replacements, and of mineral disequilibria in general, is necessary to take into account the metamorphic reactions and fluid circulation that led to partial resetting and/or growth of new mineral chronometers (Challandes *et al*. 2003, Sanchez *et al*. 2011). The ignorance of the occurrence of several mineral generations must lead (and has led) to inaccurate age estimates. To this end, we report ^{39}Ar-^{40}Ar stepwise heating results on biotite and white-mica separates from very closely spaced mylonitic micaschist samples taken near the Vaikrita Thrust, the structural top of the MCTz. A feature of ^{39}Ar-^{40}Ar dating, most useful for the present study, is its ability to characterise the analysed phases by means of the Cl/K and Ca/K ratios (Müller *et al*. 2002), and thus to diagnose the presence of heterochemical retrogression phases. This is especially valuable when attempting to date fault movements, as sheared minerals are almost always affected by re-crystallisation, dissolution/reprecipitation and alteration, and by resulting grain sizes of a few µm only (Berger *et al*. 2017). This extreme comminution strongly limits the utility of mineral separations, as it, perforce, does not allow us to produce a monomineralic separate and, thus, limits the use of *in-situ* analyses, the spatial resolution of which is often insufficient to obtain results for a single-generation mineral (Müller *et al*. 2002). The impossibility of obtaining monomineralic separates can be circumvented by a judicious use of correlation diagrams (Villa & Hanchar 2017).

Geological framework of the Garhwal Himalaya

The study area is located in the Garhwal Himalaya (Uttarakhand, NW India), where a complete structural transect across the MCTz, located between the villages of Helang and Joshimath, has been investigated (Fig. 1a,b). In this area, Valdiya (1980) and Ahmad *et al*. (2000) defined the Munsiari Thrust as the lineament at the bottom and the Vaikrita Thrust at the top of the MCTz.
Near Helang, in the southernmost portion of the transect, the Berinag Formation, belonging to Lesser Himalayan Sequence (LHS), crops out (Fig. 1b). This formation consists of schist, quartzite and carbonate rock affected by a greenschist-facies metamorphism. The main foliation strikes NW-SE and dips 30-35° to the NE (Jain *et al*. 2014).
Pervasively sheared rocks of the MCTz overlie the Berinag Formation (Fig. 1b). Within the MCTz, the Munsiari Formation crops out (Fig. 1b), consisting of Precambrian mylonitic orthogneiss, garnet-bearing micaschist, calc-silicate rock and mylonitic quartzite (Fig. 1b, Jain *et al*. 2014). The main foliation strikes from W-E to NW-SE and dips 45° from N to NE, whereas the main stretching lineation is oriented N20, 45 NE. The main kinematic indicators at the mesoscale (Jain *et al*. 2014) are S-C and S-C-C' fabrics and asymmetrical boudins pointing to a top-to-the S/SW sense of shear. At the microscale, the main kinematic indicators such as S-C fabric, σ and δ porphyroclasts and mica fish confirm a top-to-the-SW sense of shear. Th-Pb monazite ages, albeit partially decoupled from petrological and textural context, in and near the study area, suggest that the MCTz shearing lasted up to c. 6 Ma in Garhwal (Catlos *et al*. 2002). Sen *et al*. (2015) reported ^{40}Ar-^{39}Ar ages on biotite of c. 10 Ma and on muscovite of c. 6 Ma for rocks from the Vaikrita Thrust.
Spencer *et al*. (2012), in the study area, defined the Vaikrita Thrust as the MCT "*sensu stricto*" a ductile shear zone separating the lower Munsiari Formation from the upper Joshimath Formation, belonging to the Lesser Himalayan Crystalline Sequence (LHCS, Virdi 1986; Vannay & Grasemann, 1998) and the GHS, respectively. Thakur *et al*. (2015) defined the MCTz as a package of sheared rocks bounded by two discrete thrusts, namely the Munsiari Thrust at the bottom and the

Vaikrita Thrust at the top, suggesting that the MCTz in the study area corresponds to the LHCS consisting of low- to medium-grade metamorphic rocks.

Spencer *et al*. (2012) and Thakur *et al*. (2015) constrained P-T conditions of the MCTz in the study area. The data of these authors agree within the given uncertainties. Spencer *et al*. (2012) obtained P-T conditions between 0.5-1.1 GPa and 500-600° C using "classical geothermobaric methods". Thakur *et al*. (2015) obtained P-T conditions of 0.63-0.75 GPa and 550-582° C through pseudosection modeling and multi-equilibrium thermobarometry.

The Joshimath Formation, which forms the lower portion of the GHS in the study area (Fig. 1b; Spencer *et al*. 2012; Thakur *et al*. 2015), consists of paragneiss, schist, and minor calc-silicate, in which the main foliation strikes from WNW-ESE to NW-SE and dips 35-40° from N to NE (Jain *et al*. 2014). At the microscale, rocks of the Joshimath Formation show the common mineral assemblage garnet, quartz, white mica, plagioclase, biotite, staurolite, and minor kyanite. An older foliation (S_{p-1}), only locally preserved, is overprinted by the main foliation (S_p). Garnet is enveloped by the main foliation, whereas staurolite porphyroblasts are syn-kinematic and contain an internal foliation (S_i) concordant with the external one. High-temperature Grain Boundary Migration (GBM, Passchier & Trouw 2005) and minor-static recrystallisation represent the main deformation mechanisms in quartz. Kinematic indicators such as S-C-C' fabric, mica fish and σ/δ-porphyroclasts indicate a top-to-SW sense of shear.

Structurally upward, the Suraithota and Bhapkund formations represent the middle and upper GHS in the study area. The Suraithota Formation consists of kyanite-garnet-biotite-bearing gneiss, micaschist, quartzite and amphibolite intercalations (Jain *et al*. 2014). The main foliation strikes N120°-150° with a dip of 30°-40° toward NE (Jain *et al*. 2014). The Bhapkund Formation includes aluminosilicate-garnet-biotite migmatitic gneiss, tourmaline-rich leucogranitic lenses and dikes, and the Malari leucogranite, a small pluton with an age of c. 19 Ma (Sachan *et al*., 2010) outcropping at the northern margin of the Bhapkund Formation. According to Sachan *et al*. (2010), the Malari pluton is an undeformed body crosscutting the STDS. However, Spencer *et al*. (2012), Jain *et al*. (2014), Thakur *et al*. (2015), Sen *et al*. (2015) and Iaccarino *et al*. (submitted) reported that the Malari main body and the leucogranite dykes are deformed by both ductile and brittle shearing, related to the STDS.

Petrography and microstructures of selected samples

Three samples of mylonitic micaschist have been selected from the Vaikrita Thrust close to the village of Tapoban (Fig. 1b, red stars). All samples display a main schistosity, referred to as S_p, accompanied by variably identifiable rare pre-S_p relicts and/or post-S_p static mineral growth. Sample GW13-28 is a garnet-staurolite-two mica-bearing impure quartzite that also contains tourmaline, ilmenite and monazite and abundant late chlorite, partially replacing biotite and garnet. The main foliation (S_p) is defined by the shape preferred orientation (SPO) of white mica (muscovite-2), biotite (biotite-2) and ilmenite. It can be classified as disjunctive schistosity characterized by a discrete transition to domains of quartz-rich microlithons. Static recrystallisation of biotite and white mica can be also sporadically found. In the phyllosilicate-rich layers garnet porphyroclasts, enveloped by the main foliation, occur (Fig. 2a), whereas in the quartz-rich granoblastic domains garnet shows a skeleton aspect (Fig. 2b). Staurolite appears along the main foliation suggesting a syn-kinematic growth. The main recrystallisation mechanism in quartz is GBM supported by sutured and amoeboid grain boundaries. However, static annealing of quartz is sometimes present discernable by straight grain boundaries and triple points. Kinematic indicators at the microscale are represented by asymmetric recrystallisation tails of micas and asymmetric strain shadows around garnet porphyroclasts (Fig. 2a) and type 1 mica fishes (Passchier & Trouw 2005), which show a top-to-the S/SW sense of shear.

Sample GW13-29 is a mylonitic micaschist with the mineral assemblage quartz, biotite, white mica, garnet, plagioclase and ilmenite. The S_p is an anastomosing disjunctive schistosity defined by SPO of biotite (biotite-2) and white mica (muscovite-2). Locally, within the microlithons, micas (micas-1) oriented at high-angle with respect to the S_p mark an older foliation (S_{p-1}, Fig. 2c). Garnet is enveloped by the main foliation and often contains aligned inclusions of quartz, plagioclase, micas and allanitic epidote, defining an internal foliation (S_i) that is non-continuous with the external one (S_e, Fig. 2d). Thus, garnet could be classified as intertectonic porphyroblast. However, in some circumstances inclusions in garnet are not aligned. The mica-2 generation is followed structurally by a static growth of larger mica (mica-3) around garnet grains. Additional sporadic mica-3 grains are found in the matrix: they are oriented in the same direction as mica-2 but are not comminuted and suggest later, static growth by a process resembling Ostwald ripening and pseudomorphism. Relict biotite-1 and muscovite-1 may be present but are difficult to identify, as ductile deformation was very intense and has reduced the grain size of mica grains and given them a shredded appearance. It must be pointed out that recent studies (e.g. Berger *et al*. 2017, and references therein) provide conclusive observational evidence that shear-induced recrystallisation is rarely complete and results in extremely small heterochemical relict phases hosted in the recrystallised mineral matrix.

The latest generation consists of large micas (muscovite-3 and minor biotite-3) forming coronitic structures around garnet. These micas are characterised by the lack of internal deformation (undulose extinction or kinking) in contrast to mica oriented along S_p. Moreover, static recrystallisation of biotite and white mica, forming mica flakes cross-cutting S_p, took place. Main deformation mechanisms were GBM and static recrystallisation of quartz. Asymmetric recrystallisation tails of garnet porphyroclasts indicate a top-to-the-S/SW sense of shear. Sample 29 was collected < 10 m downhill from sample 28, following the road between Joshimath and Suraithota, near Tapoban.

Sample GW13-29B is a garnet-biotite-bearing mylonitic micaschist also containing quartz, white mica, plagioclase and minor chlorite. The S_p, defined by the SPO of biotite (biotite-2) and white mica (muscovite-2), can be classified as disjunctive schistosity. The microstructure is characterised by the alternation of granoblastic quartzofeldspathic layers and lepidoblastic layers. The main foliation envelops intertectonic garnet that contains aligned quartz inclusions defining an internal foliation (S_i) discordant to the external one (Fig. 2e-f). White-mica and biotite crystals (micas-3) around garnet porphyroclasts show a coronitic texture. These micas lack undulose extinction, kinking and internal deformation (Fig. 2f). These features are, instead, observed in micas-2 (Fig. 2e-f). Kinematic indicators such as δ-porphyroclasts and prevalent type 1 mica fishes (Passchier & Trouw 2005) show a top-to-SW shear sense. Sample GW13-29B was taken from an outcrop less than 1 m away from GW13-29.

Mineral chemistry of micas

Electron microprobe (EMP) analyses were carried out with a CAMECA SX100 hosted at the Institut für Mineralogie und Kristallchemie at Universität Stuttgart, equipped with five wavelength-dispersive spectrometers, using an accelerating voltage of 15 kV and a beam current of 10 nA. Details on the analytical protocol are reported in Massonne (2012). Selected analyses of the different structurally-located micas (1-3) from the studied samples are given in Table 1. Their compositional variabilities are exhibited in Figure 3.

Mineral compositions were recalculated as atoms per formula unit (apfu) on the basis of 11 and 22 oxygens for white mica and biotite, respectively.

White mica

In all three samples, white mica shows a limited compositional variation around the muscovite-celadonite join with Al ranging between 3.05 and 3.17 apfu (Fig. 3a). We detected no compositional difference between the (very rare) muscovite-1 grains and the muscovite-2 grains, which predominate by far. White mica in sample GW13-28 is characterised by Al/Si ratios higher than in the other samples (Fig. 3a). The Ti concentration (Fig. 3b) in white mica of sample GW13-28 is lower (0.007-0.023 apfu) and less scattered than in samples GW13-29 and GW13-29B. In GW13-29, muscovite-2 contains more Ti (0.030-0.043 apfu) compared to muscovite-3 (0.013-0.030 apfu, Fig. 3b). The same trend was observed in sample GW13-29B (Fig. 3b), where the Ti contents in muscovite-2 (0.023–0.036 apfu) are, however, only somewhat higher than in mica-3 (0.017-0.035 apfu).

The Na/(Na+K) ratio (Guidotti & Sassi 2002; Fig. 3c) of white mica in sample GW13-28 is higher (c. 0.12-0.14) than in samples GW13-29 and GW13-29B (0.06-0.09), which display similar trends. Muscovite-2 and muscovite-3 from sample GW13-29 have a Na/(Na+K) ratio between 0.06-0.09 and 0.06-0.08, respectively. Muscovite-2 and muscovite-3 from sample GW13-29B display similar Na/(Na+K) ratios to those of sample GW13-29 (0.06-0.08: muscovite-2; 0.07-0.08: muscovite-3).

The X_{Mg} = Mg/(Mg+Fe_{tot}) ratio is lower in muscovite-3 than in muscovite-2. In sample GW13-28 X_{Mg} ranges between 0.46 and 0.64. Muscovite-2 in sample GW13-29 shows X_{Mg} values between 0.44 and 0.50, whereas X_{Mg} of muscovite-3 is between 0.39 and 0.47. X_{Mg} in muscovite-2 and muscovite-3 of sample GW13-29B ranges between 0.44 and 0.52 and between 0.40 and 0.51, respectively.

Biotite

The mass fractions of the three biotite generations are even more lopsided than those of muscovite: biotite-1 and -3 are extremely rare. As in the case of muscovite, we detected no compositional difference between biotite-1 and biotite-2. Biotite in sample GW13-28 shows no significant chemical variation (Fig. 3d,e,f). The same concerns GW13-29, whereas in sample GW13-29B two distinct compositional clusters occur in biotite-2 (Fig. 3d,e,f, green triangles). Biotite of sample GW13-28 shows a higher X_{Mg} (0.41-0.45) than biotite in the other samples (Fig. 3d,e,f).

The Al^{IV} contents of biotite in sample GW13-28 (Fig. 3d) are more variable (2.55-2.87 apfu, Fig. 3d) than in biotite-2 and -3 of sample GW13-29 (2.53-2.66 apfu). Biotite from sample GW13-29B forms two compositional clusters discernable in X_{Mg} (0.38-0.40: biotite-2, 0.32-0.34: biotite-3) and Al^{IV} (2.57-2.60 apfu: biotite-2, 2.60-2.68 apfu: biotite-3) plots (Fig. 3).

The Ti concentrations in biotite from sample GW13-28 range between 0.12 and 0.19 apfu, whereas biotite-2 and -3 from sample GW13-29 have higher Ti contents (0.33 -0.36 apfu, except few analyses, and 0.22-0.31 apfu, respectively, Fig. 3e).

Biotite from sample GW13-29B forms two compositional clusters of biotite-2 discernable in X_{Mg} (0.33-0.34; 0.38-0.40) having the same Ti concentration (c. 0.25-0.29 apfu, Fig. 3e).

Sample GW13-29B shows two compositional clusters (Fig. 3e): one is characterised by Ti contents between 0.26 and 0.29 apfu and X_{Mg} values of 0.37-0.40 (Fig. 3e). Biotite-3 is characterised by Ti contents between 0.18 and 0.30 and X_{Mg} of 0.33-0.35.

In a diagram displaying K concentration versus X_{Mg} (Fig. 3e) sample GW13-28 has a higher X_{Mg} (0.41-0.45) with respect to the other samples. EPM analyses on grains initially supposed to be biotite from sample GW13-28 reveal K concentrations between 1.38 and 1.90 apfu, The lower concentrations clearly pertain to altered or partially altered grains, as supported by the matching element sums below 96 % for these spots. Both indicators point to a partial replacement by chlorite or smectite and confirm that this sample contains more alteration phases than the others. Both biotite-2 and -3 from sample GW13-29 are characterised by X_{Mg} between 0.32 and 0.35 at K concentrations of 1.82-1.91 apfu.

Ti-in-biotite and Ti-in-muscovite geothermometry

Methods

Thermal conditions of mica (re-)crystallisation, in regard of the different textural positions described above, were constrained through empirical geothermometers based on the Ti concentration in micas (Henry & Guidotti, 2002; Henry *et al*. 2005; Wu & Chen 2015). Several authors suggested an increase of Ti in micas with rising temperature (e.g. Henry *et al*. 2005 and reference therein; Chambers & Kohn 2012).

In the case of biotite we applied the Ti-in-biotite thermometer proposed by Henry *et al*. (2005). Henry & Guidotti (2002) and Henry *et al*. (2005), based on an extensive natural biotite dataset from graphite and rutile/ilmenite bearing samples, reconstructed a Ti-saturation surface for biotite of the P-T range of 0.4-0.6 GPa and 480-800°C. Based on this saturation surface, they proposed a relationship of T and X_{Mg} and Ti contents of biotite. The associated precision of this thermometer is ±24 °C in the lower T range, approaching ±12 °C in the higher T calibration range. The Ti-in-biotite was calibrated for the P range that is somewhat lower than the equilibration P reported previously for samples structurally close to the here studied rocks (0.82-0.88 GPa, Spencer *et al*. 2012; c. 0.73–

0.86 GPa, Thakur *et al*. 2015). In this situation, a systematic uncertainty of at least 50°C on the obtained T should be taken into account (e.g. Mottram *et al*. 2014b).

In the case of white mica we applied the pressure-dependent Ti-in-muscovite thermometer proposed by Wu & Chen (2015), who empirically calibrated this thermometer for the P-T range of 0.1-1.4 GPa and 450-800°C for ilmenite- and aluminosilicate-satured metapelite. The quoted error of the Ti-in-muscovite thermometer, as suggested by Wu & Chen (2015), is ± 65°C. We have calculated temperatures with the Ti-in-muscovite thermometer, following the assumption of a corresponding equilibrium pressure of 0.8 GPa, in agreement with the P estimates previously reported (see above). Calculation at lower P (0.6 GPa) shows only a very minor (around 5°C) decrease in the T estimates. An additional source of bias is the fact that the present rocks do not match the paragenesis used to calibrate the thermometer. Therefore, absolute temperature estimates may be inaccurate, but temperature differences between different mica generations of the same rock are probably relatively accurate.

Results

For muscovite-2, the temperatures obtained with the Ti-in-muscovite thermometer range between 394 and 561 °C, 550 and 626 °C, and 591 and 655 °C for sample GW13-28, GW13-29B, and GW13-29, respectively (Fig. S-1). These estimates are similar to, but higher than, those by Spencer *et al*. (2012) and Thakur *et al*. (2015). For samples GW13-28, GW13-29B and GW13-29, the average temperatures are 522±41 °C, 609±15 °C and 632±13 °C, respectively. Average temperatures obtained from muscovite-3 are 538±42 °C for sample GW13-29 and 571±43 °C for sample GW13-29B and, thus, systematically lower than T derived from muscovite-2.

The Ti-in-biotite geothermometer applied to biotite-2 gave average temperatures of 522±45 °C for sample GW13-28, 647±41 °C for sample GW13-29, and 627±8 °C for sample GW13-29B. The calculated T for biotite-3 is 631±18 °C and 607±27 °C for samples GW13-29 and GW13-29B, respectively, being somewhat lower than for biotite-2. The obtained temperatures for both muscovite-2 and biotite-2 from sample GW13-28 are about 90-100 °C lower than for the other samples.

The Ti-in-biotite and Ti-in muscovite geothermometers, as any geothermobarometric method (Spear 1993), are not without pitfalls (e.g. Chambers & Kohn 2012). These could be also due to kinetic problems related to the distance of micas from the Ti-source (Waters & Charnley 2002). Moreover, aluminosilicate, required for the Ti-in-muscovite thermometer, is lacking in our samples, even if other Al-rich phases such as garnet and staurolite are present as buffer, so that the Ti-in-muscovite temperature should be regarded as semi-quantitative. However, two factors strengthen our temperature estimates, at least in a semi-quantitative way, which is sufficient for the interpretation of ^{39}Ar-^{40}Ar data. Firstly, the T calculated using two different thermometers match within the corresponding uncertainties. Secondly, they are well comparable with the previously reported temperature estimates of 550-580 °C, based on the application of several geothermometric methods (e.g. garnet-biotite thermometer, Ti-in-biotite thermometer and multi-equilibrium thermobarometry) from very close samples (Spencer *et al*. 2012; 550–590 °C, Thakur *et al*. 2015).

^{39}Ar-^{40}Ar dating

Analytical techniques

Mineral separation for samples GW13-28, GW13-29, GW13-29B was performed at the Institut für Geologie at Universität Bern. The rocks were crushed and sieved. Biotite and muscovite in the sieve fraction between 150 and 350 µm were enriched with gravimetric methods and subsequently purified by extensive hand picking. Density separation of biotite was comparatively straightforward, as biotite is heavier than most major minerals of these rocks. Therefore, most biotite grains in the crushed and sieved sample were included in the separate. On the contrary, muscovite was not efficiently separable by density, and hand-picking was necessary. Only the largest and cleanest-looking grains were chosen. This operator-dependent bias is known to potentially affect samples featuring multiple deformation stages (Villa *et al*. 2014, p. 812). It is therefore expected that the shredded muscovite-2 generation was selectively left out in favour of the nearly-euhedral static muscovite-3 generation.

Mica samples were irradiated in the McMaster University Research Reactor (Hamilton, Canada) carefully avoiding Cd shielding. ^{39}Ar-^{40}Ar step-heating analyses were carried out using a double-vacuum resistance furnace attached to a NuInstruments Noblesse™ rare gas mass spectrometer at Dipartimento dell'Ambiente e della Terra, Università di Milano Bicocca. The analytical procedure of the ^{39}Ar-^{40}Ar step-heating technique is reported in Villa *et al*. (2000).

Results

The first and foremost observation is that all six age spectra (Figs. 4a, 5a) are internally discordant. Biotite ages are around 9-10 Ma, while muscovite ages are around 6 Ma. These results are apparently on a par with those reported by Sen *et al*. (2015) on nearby samples collected in the

Suraithota Formation (Fig. 1a). Moreover, the age pattern featuring older biotite ages and younger muscovite ages is also found in other MCTz localities (Jain, unpublished results; Mottram *et al.* 2015). The latter authors shrugged off the biotite ages as due to excess Ar. However, we argue that the biotite separates analysed here belong to an older mica generation than the muscovite separates, and that their ages should be viewed as inherited Ar, not as excess Ar. As these two kinds of extraneous Ar pertain to two completely different geochemical scenarios (Villa *et al*. 2014, p. 817), namely Ar loss and Ar gain, respectively, the entire interpretive framework is distorted.

Discussion

A detailed interpretation of the dating results requires the microstructural and petrogenetic context of the MCTz mylonitic schists. In contrast to the simplified discussion by Sen *et al*. (2015), we will argue that our results reflect a true diachronism based on the microstructures. This is made possible by the fact that the selected three samples share the same structural history at the 10 m scale, but record different stages of the microstructural evolution. In the following, we will first focus on the similarities and the differences of the biotite results and then discuss the muscovite results, drawing attention to the observational and interpretive constraints provided by processes affecting biotite. The biotite age spectra are not only internally discordant (Fig. 4a) but also suggest different Ar retention over an extremely small distance. This indicates that "cooling" (Sen *et al*. 2015) is unlikely to be the only factor controlling the biotite ages. Because age spectra only provide an incomplete information (Chafe *et al*. 2014), it is necessary to also take into account the information provided by the (often neglected) isotopes with masses 38 and 37, such as ^{38}Ar and ^{37}Ar, which proxy for Cl and Ca, respectively (Merrihue 1965). From the measured 38/39 and 37/39 mass ratios and the known production factors it is possible to calculate the Cl/K and Ca/K ratios, respectively (which can, but need not, be validated by EPM analyses: Villa et al. 2000). Figure 4b shows the Cl/K-Ca/K common-denominator correlation diagram (e.g. Villa & Williams 2013, and references therein). Data-points for all three samples define a very peculiar V-shaped trajectory: the first heating steps of all samples have high Ca/K and high Cl/K ratios, which monitor the degassing of calcium-rich alteration phases. At higher oven temperatures, typical of biotite *sensu stricto* degassing (c. 900 °C), Cl/K and Ca/K ratios reach a minimum and the high-temperature steps show an increase of the Ca/K ratio at constant Cl/K. This pattern applies to biotite from all three samples, but to different degrees. The only way to account for these observations is to hypothesise a three-phase mixture, whereby each sample consists of a different mass fraction of the three end-member phases. Considering the steps most closely matching the Ca-free stoichiometry of biotite, i.e. those with Ca/K < 0.001, it becomes evident that in sample GW13-28 there are none, one in sample GW13-29B, and four in GW13-29. As the micas are fine-grained and intergrown with their retrogression products at a scale < 10 µm, even handpicking did not achieve a monomineralic separate. In terms of chronological information from biotite, this unexpected observation can be used advantageously, as follows from Fig. 4c. The three biotite separates show a similar, albeit less clearly defined, V-shaped trajectory as in Fig. 4b. The interpretation in terms of a mixture of at least three phases is upheld: the alteration phase(s) having step ages up to 16 Ma and high Ca/K and high Cl/K are most abundant in sample GW13-28. The extrapolation of the age-Ca/K trend gives an apparent age > 16 Ma. This age is very likely to be geologically meaningless, because it pertains to an alteration phase: the biotite separate GW13-28 has a bulk K concentration of 4.61 %, as calculated from the total ^{39}Ar concentration**.** This low value attests a clear chloritisation of biotite in this separate. Even if the chronological information provided by GW13-28 is meaningless per se, it can provide a useful end-member constraint on the effect of alteration for the other two biotite separates, which are much less altered but not negligibly so. Indeed, in Fig. 4c the biotite separates GW13-29 and 29B follow the same pattern as in Fig. 4b, with one branch of the V-shaped trajectory pointing towards GW13-28. The four steps from GW13-29 (Fig. 4d) corresponding to the lowest Ca/K ratios, i.e. most closely approximating biotite stoichiometry, gave an isochron age of 9.07 ± 0.60 Ma (2 sigma uncertainty) with an atmospheric intercept. The atmospheric intercept allows us to consider the average age of these four steps as a legitimate "isochemical age" (Müller *et al*. 2002) of 9.00 ± 0.10 Ma. Strictly speaking, this is a cooling age, as the retention of Ar by biotite is complete only below c. 530 °C (Villa 2015). What is most important here is that biotite-2 formed several Ma earlier than muscovite-3.

In contrast to the biotite concentrates, all muscovite separates gave significantly younger ages, between c. 6 and 7 Ma. Age spectra are discordant (Fig. 5a). Muscovite from GW13-28 (with the most altered biotite) shows the most disturbed spectrum with some step ages < 5 Ma, the high Cl/K of which clearly identifies them as the degassing of alteration phases (Fig. 5a). GW 13-29B with the best preserved biotite also shows the least discordant muscovite spectrum. Common regression of the data for muscovite from GW13-29 and -29B in a single Cl/K-age diagram, justified by their spatial proximity (< 1 m), reveals a negative correlation (Fig. 5b): a relatively Cl-rich mica with an age ≤ 5.88±0.03 Ma, and a Cl-poor one, > 7 Ma old. As the microstructural observations distinguish between a fine-grained, shredded muscovite-2 along the main foliation and a coarse-grained, statically grown coronitic muscovite-3, it is very likely that hand-picking did enrich muscovite-3 compared to muscovite-2, but the respective mass fraction of the two generations in our samples are unknown. It is therefore possible that the end-member of the correlation trend seen in Fig. 5b is actually the 9.15 Ma old muscovite-2, if its mass fraction (estimated by mass balance) did not exceed 25 %.

An age difference between older biotite and younger muscovite in similar rocks was also observed by Mottram *et al*. (2015) in samples from the MCTz from Sikkim. These authors seem to accept that retention of Ar in white mica is quite high even if an ambient temperature of 600 °C was maintained over several Ma, as already documented by Di Vincenzo *et al*. (2004), Allaz *et al*. (2011) and Villa *et al*. (2014, p. 817). However, the discussion in Mottram *et al*. (2015), purely based on the assumption of thermally activated Fick's Law diffusion, is internally contradictory, as it fails to explain why biotite is reproducibly older than white mica, contrary to micas from terrains affected by a static, monometamorphic event (e.g. Allaz *et al*. 2011, and references therein). The exclusive focus on Ar diffusion in a static system also forfeits the opportunity to examine microstructures and microchemistry, and correlate both with mica ages.

Regarding Ar retention in micas, Villa *et al*. (2014) observed complete, or nearly complete, Ar retention in 100 μm sized phengite in metamorphic terrains at T > 500 °C. Villa (2015) went on to interpolate the retention of Ar in static, monometamorphic biotite and derived a revised Ar "closure temperature" estimate of c. 530 °C, in good agreement with the scarce reliable experimental data (see Villa 2010, 2015). The implication of such a high Ar retentivity for the present Garhwal samples is that biotite practically did not lose Ar by diffusion at the metamorphic temperatures recorded by fluid inclusions in quartz near the Munsiari thrust, 1 km downsection (Montemagni *et al*. 2016), namely 500-520 °C. The 9.00 ± 0.10 Ma isochemical age therefore is a cooling age closely approximating the growth of biotite-2 in sample GW13-29. *A fortiori* does the 6 Ma age, inferred from the white mica correlation diagrams, reflect the static growth of muscovite-3 during the subsequent exhumation.

Selective sampling bias due to handpicking could account for the observation of Fig. 5b, in which two anticorrelated clusters are seen in the Cl/K versus age diagram: white mica from sample GW13-28 is older and has lower Cl/K (blue dots), whereas younger white mica from samples GW13-29 and GW13-29B has higher Cl/K (pink and green dots). Mixing relatively Cl-rich static muscovite-3 with Cl-poor muscovite-2 yields a good anticorrelation of age and Cl/K ratio; the age of the foliation-parallel muscovite-2 is higher or equal to the oldest step, in the present case 7.6 Ma. By extrapolating the correlation trend towards lower Cl/K values it is possible to infer a muscovite-2 age matching the biotite-2 age of 9 Ma by assuming $Cl/K = 5 \times 10^{-5}$ for muscovite-2. The age of static mica growth is underconstrained, and we can only argue that it was less or equal to the lowest step age having the Ca/Cl/K signature of bona fide muscovite, 5.9 Ma.

In summary, syn-tectonic growth of micas-2 defining the main mylonitic foliation at c. 9 Ma constrains the age of movement of the Vaikrita Thrust. The formation of coronitic micas-3 at 5.88 Ma, post-dates the deformation due to shearing and is related to the advection of K (enabling the growth of K-mica at the expense of garnet), mediated by fluids.

Conclusions

1. The MCTz rocks in Garhwal record several well resolvable deformations. Microstructural observations show complex superposition of tectonic foliations, marked by successive mica growth and recrystallisation episodes. Microchemical analyses show both pervasive secondary alteration and primary heterogeneity of biotite. Muscovite is less altered and less clearly heterogeneous.
2. Three different generations of micas were observed: mica-1 in a relict foliation at high-angle with respect to the main mylonitic one (Sp); mica-2, oriented along S_p, is characterised by small flakes of both muscovite and biotite; mica-3, consisting of large crystals of muscovite and rare biotite, in coronitic structures around garnet porphyroclasts. Mica-3 lacks undulose extinction; its microstructure and chemical composition suggest formation during garnet breakdown.
3. ^{39}Ar-^{40}Ar age spectra are discordant and show both inter- and intra-sample discrepancies, which cannot be interpreted as “cooling age” differences, as samples from the same outcrop cooled simultaneously. Instead, Ar systematics reflect sample-specific markers of heterochemical recrystallisation. The isochron age of biotite *sensu stricto* is 9.07 ± 0.60 Ma. Muscovite shows a negative correlation between the Cl/K ratio and age as a result of a mixture of a relatively Cl-rich mica (muscovite-3?), 5.88±0.03 Ma old, and a Cl-poor one, > 7 Ma old. The extrapolation of the correlation trend to low Cl/K values allows to define, but not to constrain, an end-member (muscovite-2) to be as old as ≈ 9 Ma.
4. Combining all data, we propose the following evolution: syntectonic growth of mica-2 occurred along the main foliation at c. 9 Ma; the formation of coronitic muscovite at 5.88 Ma post-dated the deformation due to shearing along the Vaikrita Thrust; minor to pervasive alteration of muscovite occurred before, during and after coronite growth.

References

AHMAD, T., HARRIS, N., BICKLE, M., CHAPMAN, H., BUNBORY, J. & PRINCE, C. 2000. Isotopic constraints on the structural relationship between the Lesser Himalayan Series and the High

Himalayan Crystalline Series, Garhwal Himalaya. *Geological Society of America Bulletin,* **112**, 467-477.

ALLAZ, J., ENGI, M., BERGER, A. & VILLA, I. M. 2011. The effects of retrograde reactions and of diffusion on ^{40}Ar–^{39}Ar ages of micas. *Journal of Petrology*, **52(4)**, 691-716.

ARITA, K., 1983. Origin of the inverted metamorphism of the lower Himalaya, central Nepal. *Tectonophysics*, **95,** 43-60.

BERGER, A., WEHRENS, P., LANARI, P., ZWINGMANN H. & HERWEGH, M. 2017. Microstructures, mineral chemistry and geochronology of white micas along a retrograde evolution: An example from the Aar massif (Central Alps, Switzerland). *Tectonophysics*, in press.

CAROSI, R., MONTOMOLI, C. & VISONÀ, D. 2002. Is there any detachment in the Lower Dolpo (Western Nepal)? *Comptes Rendus Geoscience*, **334**, 933–940.

CAROSI, R., MONTOMOLI, C., RUBATTO, D. & VISONÀ, D. 2006. Normal-sense shear zones in the core of the Higher Himalayan Crystallines (Bhutan Himalaya): Evidence for extrusion?. *Geological Society, London, Special Publications*, **268**, 425-444.

CAROSI, R., MONTOMOLI, C. & VISONÀ, D. 2007. A structural transect in the Lower Dolpo: insights on the tectonic evolution of Western Nepal. *Journal of Asian Earth Sciences*, **29**, 407-423.

CAROSI, R., MONTOMOLI, C., RUBATTO, D. VISONÀ, D. 2010. Late Oligocene high-temperature shear zones in the core of the Higher Himalayan Crystallines (Lower Dolpo, Western Nepal), *Tectonics*, **29**, TC4029, doi: 10.1029/2008TC002400.

CAROSI, R., MONTOMOLI, C., IACCARINO, S., MASSONNE, H. -J., RUBATTO, D., LANGONE, A., GEMIGNANI, L. & VISONÀ, D. 2016. Middle to late Eocene exhumation of the Greater Himalayan Sequence in the Central Himalayas: Progressive accretion from the Indian plate. *Geological Society of America Bulletin*, **128(11-12)**, 1571-1592.

CATLOS, E. J., HARRISON, T. M., MANNING, C. E., GROVE, M., RAI, S. M., HUBBARD, M. S. & UPRETI, B. N. 2002. Records of the evolution of the Himalayan orogen from in situ Th–Pb microprobe dating of monazite: Eastern Nepal and western Garhwal. *Journal of Asian Earth Sciences*, **20**, 459-479.

CÉLÉRIER, J., HARRISON, T. M., BEYSSAC, O., HERMAN, F., DUNLAP, W. J. & WEBB, A. A. G. 2009. The Kumaun and Garwhal Lesser Himalaya, India; Part 2. Thermal and deformation histories. *Geological Society of America Bulletin*, **121**, 1281-1297.

CHAFE, A. N., VILLA, I. M., HANCHAR, J. M. & WIRTH, R. 2014. A re-examination of petrogenesis and ^{40}Ar/^{39}Ar systematics in the Chain of Ponds K-feldspar: "diffusion domain" archetype versus polyphase hygrochronology. *Contributions to Mineralogy and Petrology,* **167**, 1010, doi: 10.1007/s00410-014-1010-x.

Challandes, N., Marquer, D. & Villa, I. M. 2003. Dating the evolution of C–S microstructures: a combined $^{40}Ar/^{39}Ar$ step-heating and UV laserprobe analysis of the Alpine Roffna shear zone. *Chemical Geology*, **197**, 3-19.

Chambers, J. A. & Kohn, M. J. 2012. Titanium in muscovite, biotite, and hornblende: Modeling, thermometry, and rutile activities of metapelites and amphibolites. *American Mineralogist*, **97(4)**, 543-555.

Colchen, M., Le Fort, P. & Pêcher, A. 1986. Carte Géologique Annapurna– Manaslu–Ganesh, Himalaya du Nepal. *CNRS, Paris*, pp. 136.

Cottle, J. M., Searle, M. P., Jessup, M. J., Crowley, J. L. & Law, R. D. 2015. Rongbuk re-visited: Geochronology of leucogranites in the footwall of the South Tibetan Detachment System, Everest Region, Southern Tibet. *Lithos*, 227, 94-106, doi: http://dx.doi.org/10.1016/j.lithos.2015.03.019.

DeCelles, P. G., Gehrels, G. E., Quade, J., Lareau, B. & Spurlin, M. 2000. Tectonic implications of U–Pb zircon ages of the Himalayan orogenic belt in Nepal. *Science*, **288**, 497-499.

Di Vincenzo, G., Carosi, R. & Palmeri, R. (2004). The relationship between tectono-metamorphic evolution and argon isotope records in white mica: constraints from in situ $^{40}Ar–^{39}Ar$ laser analysis of the Variscan basement of Sardinia. *Journal of Petrology*, ***45*(5)**, 1013-1043.

Godin, L., Grujic, D., Law, R. D. & Searle, M. P. 2006.Channel flow, ductile extrusion and exhumation in continental collision zones: an introduction. *In*: Law, R. D., Searle, M. P. & Godin, L. (eds) *Channel Flow, Ductile Extrusion and Exhumation in Continental Collision Zones*. Geological Society, London, Special Publications, **268**, 1–23.

Guidotti, C.V. & Sassi F. P. 2002. Constraints on studies of metamorphic K-Na white micas. In: Micas: Crystal Chemistry & Metamorphic Petrology, *Reviews in Mineralogy and Geochemistry,* **46***,* 413-448.

Gupta, S., Das, A., Goswami, S., Modak, A. & Mondal, S. 2010. Evidence for structural discordance in the inverted metamorphic sequence of Sikkim Himalaya: towards resolving the Main Central Thrust controversy. *Journal of the Geological Society of India*, **75**, 313–322.

Heim, A. A. & Gansser, A. 1939. Central Himalaya: Geological observations of the Swiss Expedition, 1936. *Delhi, India, Hindustan Publishing*, pp. 26.

Henry, D. J., & Guidotti, C. V. 2002. Titanium in biotite from metapelitic rocks: Temperature effects, crystal-chemical controls, and petrologic applications. *American Mineralogist*, **87(4)**, 375-382.

Henry, D. J., Guidotti, C. V. & Thomson, J. A. 2005. The Ti-saturation surface for low-to-medium pressure metapelitic biotites: Implications for geothermometry and Ti-substitution mechanisms. *American Mineralogist*, **90(2-3)**, 316-328.

Iaccarino, S., Montomoli, C., Carosi, R., Massonne, H.-J., Langone, A. & Visonà, D. 2015. Pressure–temperature–time–deformation path of kyanite-bearing migmatitic paragneiss in the Kali Gandaki valley (Central Nepal): Investigation of Late Eocene–Early Oligocene melting processes. *Lithos,* **231**, 103-121.

Iaccarino, S., Montomoli, C., Carosi, R., Massonne, H.-J. & Visonà, D. 2017. Geology and tectono-metamorphic evolution of the Himalayan metamorphic core: insights from the Mugu Karnali transect, Western Nepal (Central Himalaya). *Journal of Metamorphic Geology*, doi:10.1111/jmg.12233.

Jain, A. K., Shreshtha, M., Seth, P., Kanyal, L., Carosi, R., Montomoli, C., Iaccarino, S. & Mukherjee, P. K. 2014. The Higher Himalayan Crystallines, Alaknanda – Dhauli Ganga Valleys, Garhwal Himalaya, India. *In*: Montomoli, C., Carosi, R., Law, R., Singh, S. & Rai, S.M. (eds) *Geological field trips in the Himalaya, Karakoram and Tibet*. Journal of the Virtual Explorer Electronic Edition, **47**.

Larson, K. P. & Godin, L. 2009. Kinematics of the Greater Himalayan sequence, Dhaulagiri Himal: implications for the structural framework of central Nepal. *Journal of the Geological Society*, **166**, 25-43.

Martin, A. J. 2016. A review of definitions of the Himalayan Main Central Thrust. *International Journal of Earth Science*, doi:10.1007/s00531-016-1419-8.

Massonne, H. -J. 2012. Formation of amphibole and clinozoisite–epidote in eclogite owing to fluid infiltration during exhumation in a subduction channel. *Journal of Petrology*, **53(10)**, 1969-1998.

Merrihue, C. M. 1965. Trace-element determinations and potassium-argon dating by mass spectroscopy of neutron-irradiated samples. *Transactions of the American Geophysical Union*, **46**, 125.

Metcalfe, R. P. 1993. Pressure, temperature and time constraints on metamorphism across the Main Central Thrust zone and High Himalayan Slab in the Garhwal Himalaya. *Geological Society, London, Special Publications*, **74(1)**, 485-509.

Montemagni, C., Fulignati, P., Iaccarino, S., Marianelli, P., Montomoli, C. & Sbrana, A. 2016. Deformation and fluid flow in the Munsiari Thrust (NW India): a preliminary fluid inclusion study. *Atti Società Toscana Scienze Naturali*, doi: 10.2424/ASTSN.M.2016.22.

Montomoli, C., Carosi, R. & Iaccarino, S. 2015. Tectonometamorphic discontinuities in the Greater Himalayan Sequence: a local or a regional feature? *In*: Mukherjee, S., van der Beek, P.

& Mukherjee, P.K. (eds) *Tectonics of the Himalaya*. Geological Society, London, Special Publications, **412**, 21-41, doi: 10.1144/SP412.3.

MONTOMOLI, C., IACCARINO, S., CAROSI, R., LANGONE, A. & VISONÀ, D. 2013. Tectonometamorphic discontinuities within the Greater Himalayan Sequence in Western Nepal (Central Himalaya): Insights on the exhumation of crystalline rocks. *Tectonophysics*, **608**, 1349-1370.

MOTTRAM, C. M., ARGLES, T. W., HARRIS, N. B. W., PARRISH, R. R., HORSTWOOD, M. S. A., WARREN, C. J. & GUPTA, S. 2014a. Tectonic interleaving along the Main Central Thrust, Sikkim Himalaya. *Journal of the Geological Society,* **171**, 255–268.

MOTTRAM, C. M., PARRISH, R. R., REGIS, D., WARREN, C. J., ARGLES, T. W., HARRIS, N. B. & ROBERTS, N. M. 2015. Using U- Th- Pb petrochronology to determine rates of ductile thrusting: Time windows into the Main Central Thrust, Sikkim Himalaya. *Tectonics*, **34**, 1355-1374.

MOTTRAM, C. M., WARREN, C. J., REGIS, D., ROBERTS, N. M., HARRIS, N. B., ARGLES, T. W. & PARRISH, R. R. 2014b. Developing an inverted Barrovian sequence; insights from monazite petrochronology. *Earth and Planetary Science Letters*, **403**, 418-431.

MUKHOPADHYAY, D. K., CHAKRABORTY, S., TREPMANN, C., RUBATTO, D., ANCZKIEWICZ, R., GAIDIES, F., DASGUPTA, S. & CHOWDHURY, P. 2017. The nature and evolution of the Main Central Thrust: Structural and geochronological constraints from the Sikkim Himalaya, NE India. *Lithos*, doi:10.1016/j.lithos.2017.01.015.

MÜLLER, W., KELLEY, S. P. & VILLA, I. M. 2002. Dating fault-generated pseudotachylytes: Comparison of $^{40}Ar/^{39}Ar$ stepwise-heating, laser-ablation and Rb-Sr microsampling analyses. *Contributions to Mineralogy and Petrology*, **144**, 57-77.

PASSCHIER, C. W. & TROUW, R. A. J. 2005. Microtectonics. *Second Edition*. *Springer, Berlin*.

ROBINSON, D. M. 2008. Forward modeling the kinematic sequence of the central Himalayan thrust belt, western Nepal. *Geosphere*, **4**, 785-801.

ROBINSON, D. M., DECELLES, P. G., GARZIONE, C. N., PEARSON, O. N., HARRISON, T. M. & CATLOS, E. J. 2001. The kinematic evolution of the Nepalese Himalaya interpreted from Nd isotopes. *Earth and Planetary Science Letters*, **192**, 507-521.

ROLLAND, Y., COX, S. F. & CORSINI, M. 2009. Constraining deformation stages in brittle–ductile shear zones from combined field mapping and $^{40}Ar/^{39}Ar$ dating: the structural evolution of the Grimsel Pass area (Aar Massif, Swiss Alps). *Journal of Structural Geology*, **31**, 1377-1394.

SACHAN, H. K., KOHN, M. J., SAXENA, A. & CORRIE, S. L. 2010. The Malari leucogranite, Garhwal Himalaya, northern India: chemistry, age, and tectonic implications. *Geological Society of America Bulletin*, **122**, 1865-1876.

Saklani, P. S., Nainwal, D. C. & Singh, V. K. 1991. Geometry of the composite Main Central Thrust (MCT) in the Yamuna Valley, Garhwal Himalaya, India. *Neues Jahrbuch für Geologie und Palaeontologie: Monatshefte*, **6**, 364-380.

Sanchez, G., Rolland, Y., Schneider, J., Corsini, M., Oliot, E., Goncalves, P., Verati, C., Lardeaux, J. -M. & Marquer, D. 2011. Dating low-temperature deformation by ^{40}Ar/^{39}Ar on white mica, insights from the Argentera-Mercantour Massif (SW Alps). *Lithos*, **125**, 521-536.

Searle, M. P., Law, R. D., Godin, L., Larson, K. P., Streule, M. J., Cottle, J. M. & Jessup, M. J. 2008. Defining the Himalayan Main Central Thrust in Nepal. *Journal of the Geological Society, London*, **165,** 523-534.

Sen, K., Chaudhurya, R. & Pfänder, J. 2015. ^{40}Ar–^{39}Ar age constraint on deformation and brittle–ductile transition of the Main Central Thrust and the South Tibetan Detachment zone from Dhauliganga valley, Garhwal Himalaya, India. *Journal of Geodynamics*, **88**, 1-13.

Spencer, C. J., Harris, R. A. & Dorais, M. J. 2012. The metamorphism and exhumation of the Himalayan metamorphic core, eastern Garhwal region, India. *Tectonics*, **31**, 1-18.

Thakur, S. S., Patel, S. C. & Singh, A. K. 2015. A P-T pseudosection modelling approach to understand metamorphic evolution of the Main Central Thrust Zone in the Alaknanda valley, NW Himalaya. *Contribution to Mineralogy and Petrology*, **170**, 1-26.

Valdiya, K. S. 1980. The two intracrustal boundary thrusts of the Himalaya. *Tectonophysics*, **66**, 323-348.

Vance, D., Müller, W. & Villa, I. M. (2003). Geochronology: linking the isotopic record with petrology and textures—an introduction. In: Vance, D., Müller, W. & Villa, I. M. (eds) *Geochronology: Linking the Isotopic Record with Petrology and Textures*. Geological Society, London, Special Publications, **220**, 1-24.

Villa, I. M. 2010. Disequilibrium textures versus equilibrium modelling: geochronology at the crossroads. *Geological Society, London, Special Publications*, **332**, 1-15.

Villa, I. M. 2015. ^{39}Ar-^{40}Ar geochronology of mono-and polymetamorphic basement rocks. *Periodico di mineralogia*, **84**, 615-632.

Villa, I. M. & Hanchar, J.M. 2017. Age discordance and mineralogy. *American Mineralogist,* in revision

Villa, I. M. & Williams, M. L. 2013. Geochronology of metasomatic events. In: Harlov, D. E. & Austrheim, H. (eds) *Metasomatism and the Chemical Transformation of Rock*. Springer, Heidelberg, pp. 171–202.

VILLA, I. M., HERMANN, J., MÜNTENER, O. & TROMMSDORFF, V. 2000. $^{39}Ar–^{40}Ar$ dating of multiply zoned amphibole generations (Malenco, Italian Alps). *Contributions to Mineralogy and Petrology*, **140(3)**, 363-381.

VILLA, I. M., BUCHER, S., BOUSQUET, R., KLEINHANNS, I.C. & SCHMID, S.M. 2014. Dating polygenetic metamorphic assemblages along a transect across the Western Alps. *Journal of Petrology*, **55**, 803-830.

VIRDI, N. S. 1986. Lithostratigraphy and structure of Central Crystallines in the Alaknanda and Dhauliganga valleys of Garhwal U.P. Himalayan thrusts and associated rocks. In: Saklani, P. S. (eds) *Current trends in geology*, **10**, 155–166.

WATERS, D. J. & CHARNLEY, N. R. 2002. Local equilibrium in polymetamorphic gneiss and the titanium substitution in biotite. *American Mineralogist*, **87(4)**, 383-396.

WEINBERG, R. F. 2016. Himalayan leucogranites and migmatites: nature, timing and duration of anataxis, *Journal of Metamorphic Geology,* **34***,* 821-843.

WU, C. M. & CHEN, H. X. 2015. Calibration of a Ti-in-muscovite geothermometer for ilmenite-and Al_2SiO_5-bearing metapelites. *Lithos*, **212**, 122-127.

Figure captions

Fig. 1: simplified geological map of (a) the Himalayas after Weinberg (2016) and (b) study area (after Jain *et al*. 2014). Red stars indicate the position of analysed samples.

Fig. 2: microstructures of the Vaikrita Thrust. (a) garnet porphyroclast wrapped by the main foliation (S_p) , shows a top-to-SW sense of shear (sample GW13-28); (b) chloritisation of biotite (sample GW13-28); (c) Sp and relict Sp-1 in mylonitic micaschist (sample GW13-29); (d) intertectonic garnet in sample GW13-29. Note the internal foliation (S_i) in garnet and the coronitic micas (white arrows); (e) δ-type garnet porphyroclast, displays a top-to-SW sense of shear, (sample GW13-29B); (f) detail of the black box in Fig. 2e. Note non deformed coronitic micas and deformed micas on the S_p (white arrows), intertectonic garnet shows a S_i discordant with respect to the S_p (sample GW13-29B). Mineral abbreviations: Bt – biotite, Grt – garnet, Qz– quartz, St – staurolite, Tur – torumaline, Wm – white mica.

Fig. 3: compositional variations in white mica (a-c) and biotite (d-f). Symbols in (b-f) are the same in (a).

Fig. 4: (a) ^{39}Ar-^{40}Ar age spectra of biotite comparing the three samples of the Vaikrita Thrust; (b) V-shaped trajectory of Cl/K vs Ca/K diagram. In the black box are highlighted the reliable low Ca – low Cl analyses, the dashed lines represent two trends: low Cl – variable Ca of the alteration phases of sample GW13-28 and variable Cl – low Ca trend; (c) age vs Cl/K correlation diagram of sample GW13-29 and GW13-29B. The dotted line contains the reliable analyses; (d) isochron obtained with the best four steps of sample GW13-29, corresponding to analyses contained in the dotted circle in (c).

Fig. 5: (a) ^{39}Ar-^{40}Ar age spectra of muscovite comparing the three samples of the Vaikrita Thrust. (b) Age vs Cl/K correlation diagram reveals a negative correlation between a Cl-rich mica, representing the coronitic white mica, and a Cl-poor one, possibly representing white mica along the S_p. Musc-2 – white mica along the Sp; Musc-3 – coronitic white mica around garnet.

Fig. S-1: histograms reporting thermometric data obtained with Ti-in-biotite and Ti-in-muscovite geothermometers. (a) and (c): data on white mica along the S_p (white mica-2) and coronitic around garnet (white mica-3), respectively; (b) and (d) data on biotite along the S_p (biotite-2) and coronitic around garnet (biotite-3), respectively. The legend in (b-d) is the same in (a).

Table captions

Table 1: representative electron microprobe analyses of white mica and biotite

Supplementary Table 1: ^{39}Ar-^{40}Ar data

Table 1

	Sample 28						Sample 29								Sample 29B							
	Muscovite			Biotite			Muscovite				Biotite				Muscovite				Biotite			
	Sp	Sp	Sp	Sp	Sp	Sp	cor.	cor.	Sp	Sp	cor.	cor.	Sp	Sp	cor.	cor.	Sp	Sp	cor.	cor.	Sp	Sp
SiO_2	46.14	46.27	46.00	34.36	34.98	33.54	45.37	46.09	45.79	45.64	34.28	34.28	34.60	34.50	44.98	46.17	45.62	45.13	33.99	34.31	34.13	35.00
TiO_2	0.44	0.45	0.39	1.52	1.27	1.55	0.49	0.29	0.77	0.79	2.48	2.36	3.07	3.04	0.33	0.47	0.72	0.68	1.56	1.86	2.33	2.52
Al_2O_3	33.79	34.06	33.85	18.82	18.93	19.16	33.46	33.93	32.42	32.41	17.27	17.15	17.24	16.90	33.98	34.26	33.08	32.77	18.16	17.47	17.40	17.91
FeO_{tot}	1.41	1.01	1.12	21.69	20.86	21.14	2.04	1.91	2.26	2.22	23.15	23.22	23.23	23.07	1.97	1.99	2.19	2.19	24.39	24.47	24.13	22.19
MnO	b.d.	b.d.	b.d.	0.05	0.04	0.01	b.d.	0.01	b.d.	b.d.	0.16	0.15	0.18	0.12	0.01	b.d.	0.01	b.d.	0.07	0.01	0.07	b.d.
MgO	1.06	0.91	1.00	8.82	8.64	9.78	0.83	0.89	1.18	1.08	6.67	6.86	6.87	6.84	0.77	0.91	1.05	1.04	7.22	7.11	6.90	8.04
CaO	b.d.	b.d.	0.01	b.d.	0.03	0.03	b.d.	0.01	b.d.	b.d.	0.01	0.01	b.d.	b.d.	0.02	b.d.	b.d.	b.d.	b.d.	0.01	b.d.	b.d.
BaO	0.19	0.13	0.19	0.11	0.05	0.06	0.30	0.27	0.31	0.31	0.15	0.13	0.15	0.25	0.24	0.24	0.21	0.21	0.10	0.13	0.18	0.20
Na_2O	0.90	0.92	0.91	0.07	0.28	0.06	0.59	0.65	0.54	0.56	0.13	0.08	0.16	0.15	0.58	0.62	0.62	0.49	0.09	0.09	0.07	0.08
K_2O	10.21	9.68	10.01	8.96	9.38	7.59	10.92	10.66	10.97	10.39	9.44	9.58	9.27	9.61	10.90	10.88	10.82	10.71	9.41	9.74	9.72	9.74
F	b.d.	0.05	0.09	0.29	0.38	0.18	0.05	b.d.	0.17	0.05	0.21	0.25	0.13	0.15	b.d.	b.d.	b.d.	0.08	0.28	0.04	0.19	0.24
Cl	b.d.	0.01	b.d.	0.04	0.12	0.04	b.d.	b.d.	b.d.	b.d.	0.03	0.02	0.02	0.02	0.01	b.d.	b.d.	0.01	0.03	0.03	0.02	0.03
Tot	94.15	93.49	93.58	94.73	94.94	93.13	94.05	94.70	94.42	93.44	93.96	94.08	94.92	94.65	93.79	95.53	94.31	93.32	95.30	95.25	95.15	95.96
Si	3.12	3.13	3.12	5.33	5.39	5.24	3.09	3.11	3.12	3.13	5.43	5.43	5.42	5.43	3.07	3.09	3.10	3.10	5.33	5.40	5.37	5.39
Ti	0.02	0.02	0.02	0.18	0.15	0.18	0.03	0.01	0.04	0.04	0.30	0.28	0.36	0.36	0.02	0.02	0.04	0.04	0.18	0.22	0.28	0.29
Al	2.69	2.71	2.70	3.44	3.44	3.53	2.69	2.70	2.60	2.62	3.23	3.20	3.18	3.14	2.74	2.70	2.65	2.65	3.36	3.24	3.23	3.25
Fe	0.08	0.06	0.06	2.81	2.69	2.76	0.12	0.11	0.13	0.13	3.07	3.08	3.04	3.04	0.11	0.11	0.12	0.13	3.20	3.22	3.18	2.86
Mn	--	--	--	0.01	0.00	0.00	--	0.00	--	--	0.02	0.02	0.02	0.02	0.00	--	0.00	--	0.01	0.00	0.01	--
Mg	0.11	0.09	0.10	2.04	1.98	2.28	0.08	0.09	0.12	0.11	1.57	1.62	1.60	1.61	0.08	0.09	0.11	0.11	1.69	1.67	1.62	1.85
Ca	--	--	0.00	--	0.00	0.01	--	0.00	--	--	0.00	0.00	--	--	0.00	--	--	--	--	0.00	--	--
Ba	0.00	0.00	0.01	0.01	0.00	0.00	0.01	0.01	0.01	0.01	0.01	0.01	0.01	0.02	0.01	0.01	0.01	0.01	0.01	0.01	0.01	0.01
Na	0.12	0.12	0.12	0.02	0.08	0.02	0.08	0.08	0.07	0.07	0.04	0.02	0.05	0.05	0.08	0.08	0.08	0.07	0.03	0.03	0.02	0.02
K	0.88	0.83	0.87	1.77	1.84	1.51	0.95	0.92	0.95	0.91	1.91	1.94	1.85	1.93	0.95	0.93	0.94	0.94	1.88	1.95	1.95	1.91
F	--	0.01	0.02	0.14	0.19	0.09	0.01	--	0.04	0.01	0.10	0.13	0.06	0.08	--	--	--	0.02	0.14	0.02	0.10	0.12
Cl	--	0.00	--	0.01	0.03	0.01	--	--	--	--	0.01	0.01	0.01	0.01	0.00	--	--	0.00	0.01	0.01	0.01	0.01
Tot	7.02	6.98	7.01	15.75	15.81	15.63	7.06	7.03	7.07	7.02	15.69	15.73	15.61	15.67	7.05	7.04	7.05	7.05	15.83	15.77	15.77	15.72

Atoms per formula unit are based on 11 oxygens for white mica and 22 for biotite. Abbreviation: Sp - micas on the main foliation; cor - coronitic micas around garnet; b.d. – below detection limit.

Figure 1

Click here to download Figure Montemagni et al._Fig.1.pdf

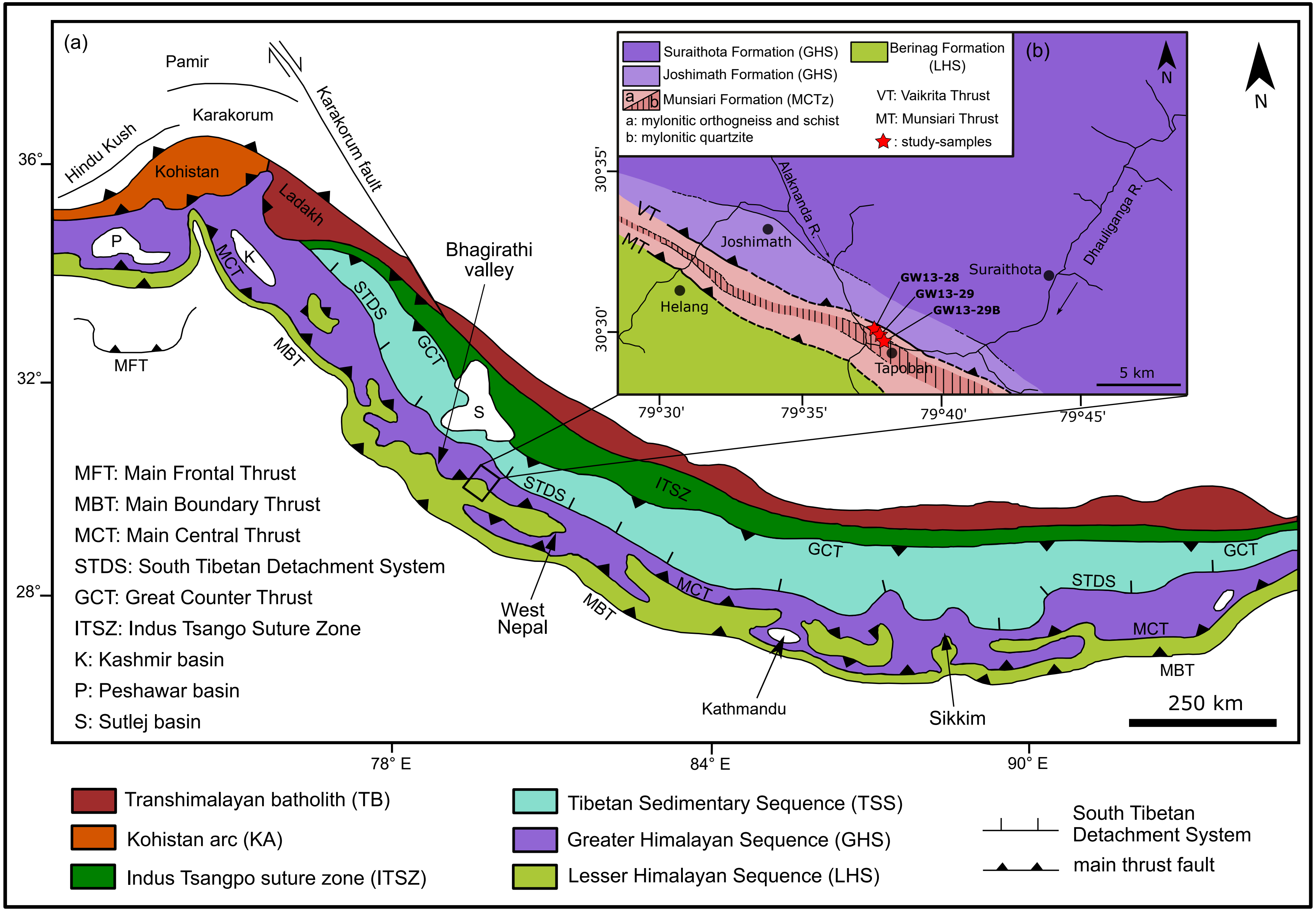

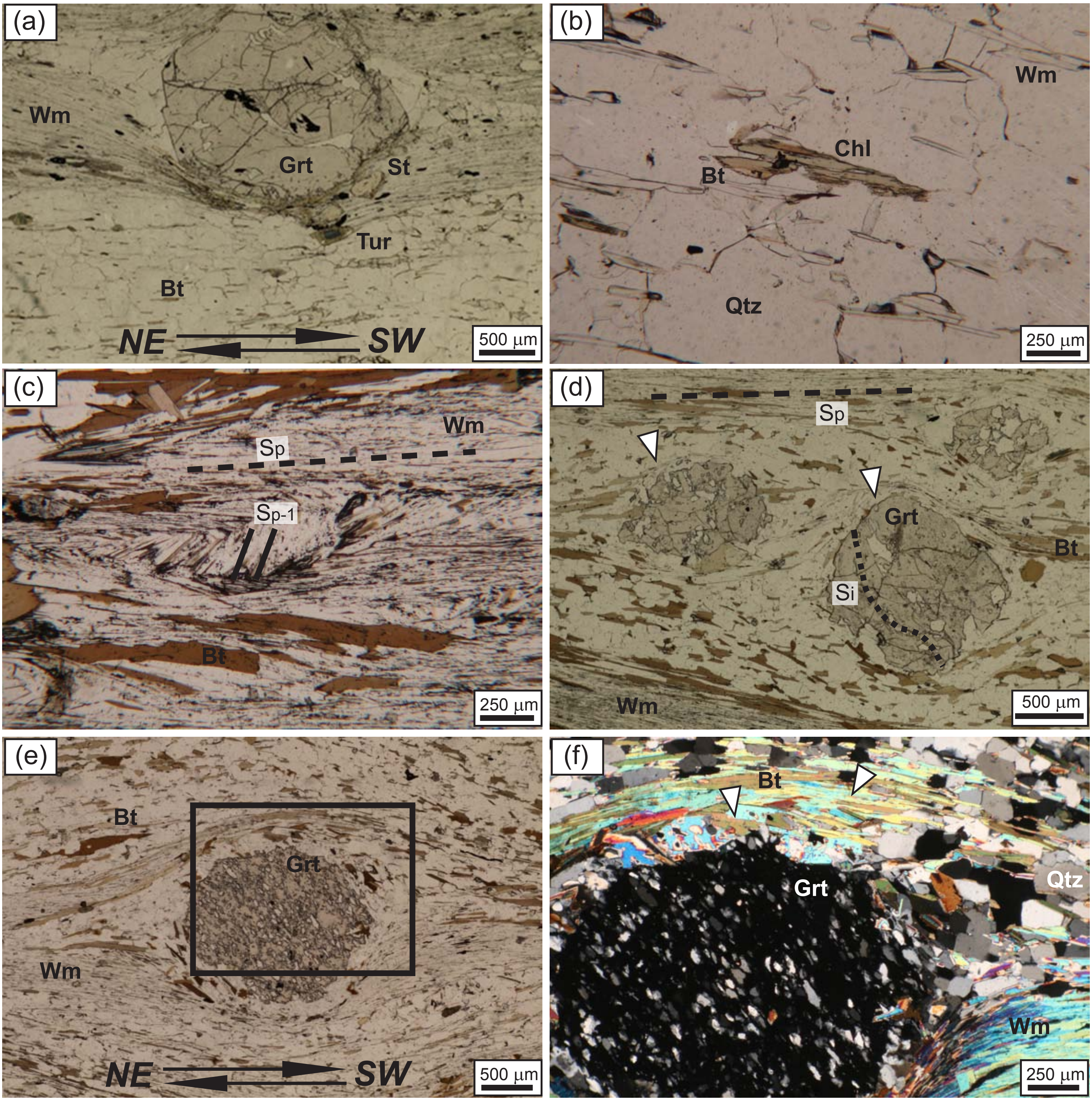
(a)
Wm
Grt
St
Tur
Bt
NE
SW
500 μm
(b)
Wm
Chl
Bt
Qtz
250 μm
(c)
Wm
Sp
Sp-1
Bt
250 μm
(d)
Sp
Grt
Bt
Si
Wm
500 μm
(e)
Bt
Grt
Wm
NE
SW
500 μm
(f)
Bt
Grt
Qtz
Wm
250 μm

Figure 3

Click here to download Figure Montemagni et al._Fig.3.pdf

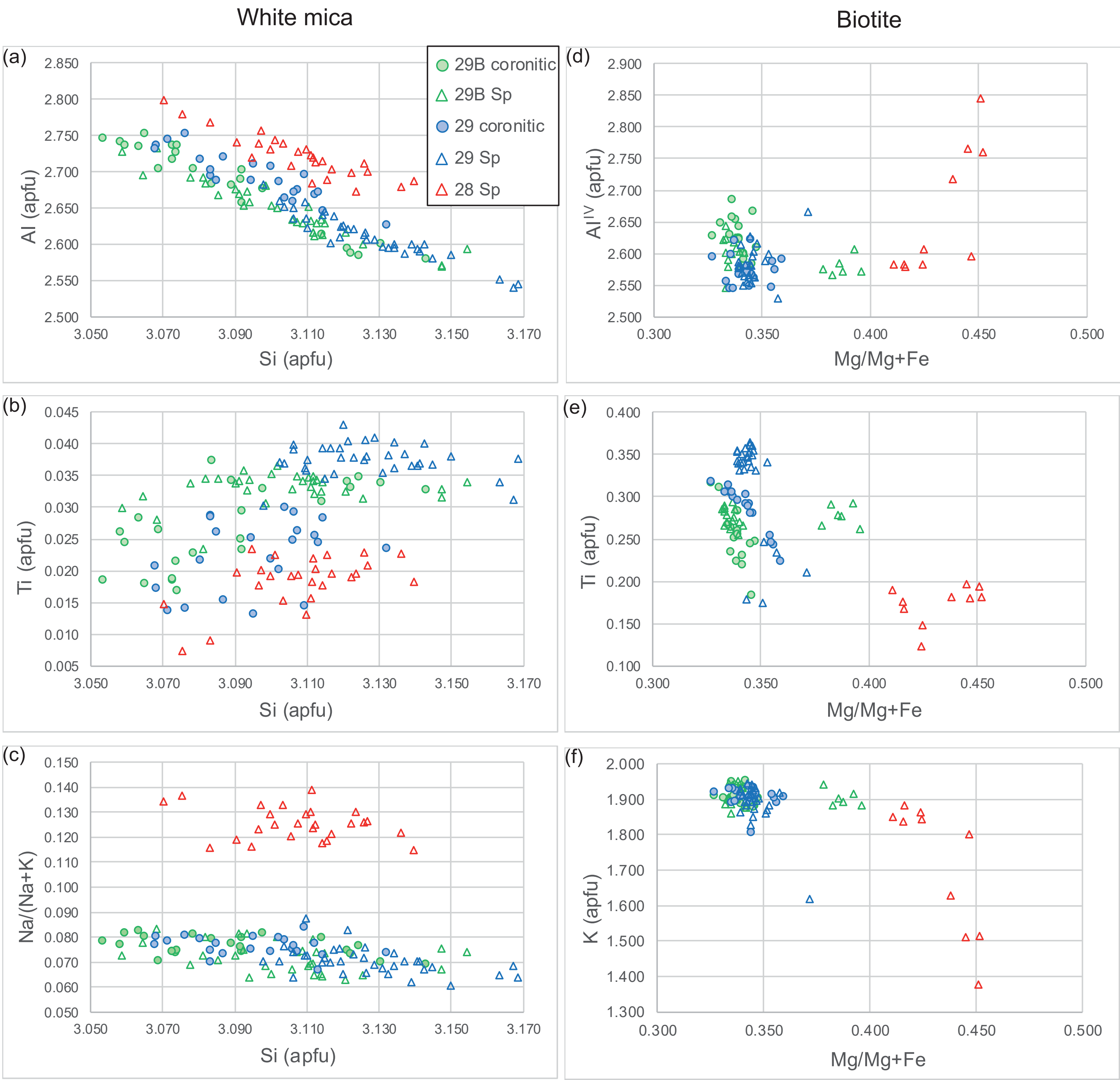

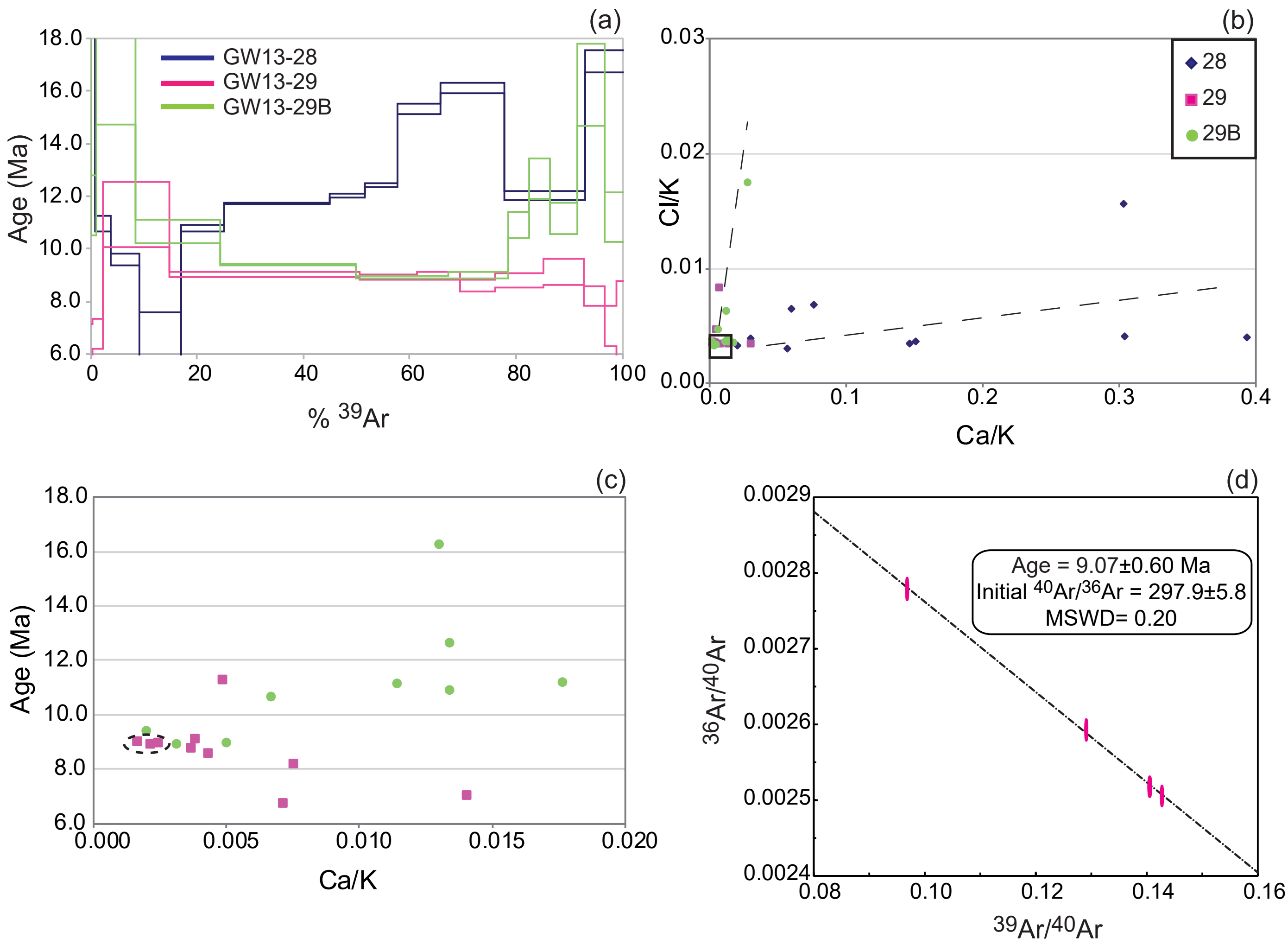
(a)
GW13-28
GW13-29
GW13-29B
Age (Ma)
% 39Ar
(b)
28
29
29B
Cl/K
Ca/K
(c)
Age (Ma)
Ca/K
(d)
Age = 9.07±0.60 Ma
Initial 40Ar/36Ar = 297.9±5.8
MSWD= 0.20
36Ar/40Ar
39Ar/40Ar

Figure 5

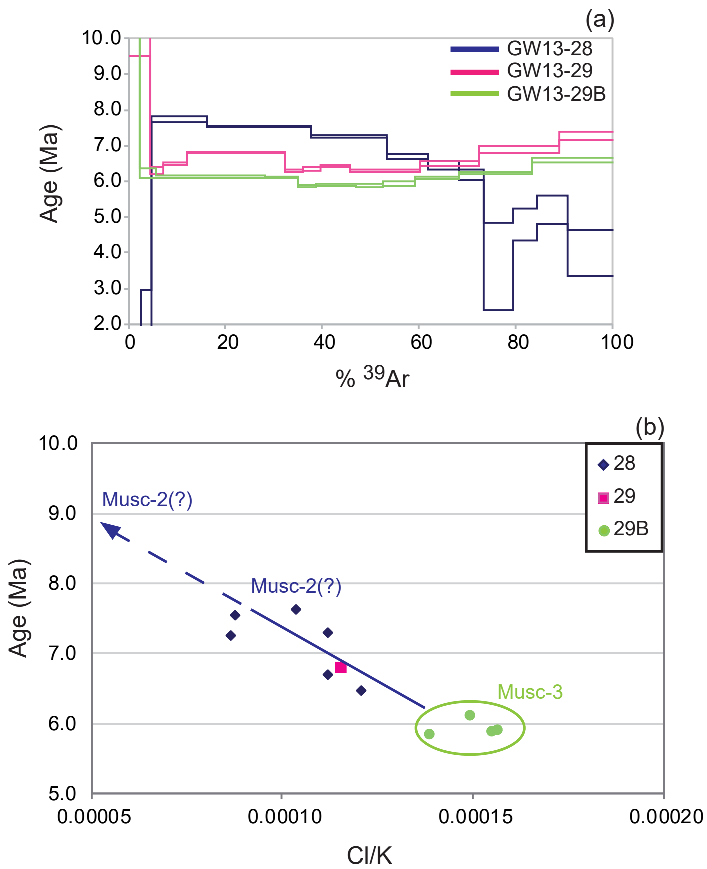
(a)
GW13-28
GW13-29
GW13-29B
Age (Ma)
10.0
9.0
8.0
7.0
6.0
5.0
4.0
3.0
2.0
0
20
40
60
80
100
% 39Ar
(b)
28
29
29B
Musc-2(?)
Musc-2(?)
Musc-3
Age (Ma)
10.0
9.0
8.0
7.0
6.0
5.0
0.00005
0.00010
0.00015
0.00020
Cl/K

Click here to access/download
Dataset
Montemagni et al_Ar-Ar dataset.xlsx

Supplementary material: Figure

Click here to access/download
Supplementary material (not datasets)
Montemagni et al._SupplementaryFigure.pdf